Global and Planetary Change

Shallow ocean oxygen decline during the end-Triassic mass extinction

--Manuscript Draft--

Manuscript Number:	GLOPLACHA-D-21-00635
Article Type:	VSI:Hyperthermal
Keywords:	Shallow ocean deoxygenation; Western Tethys; End-Triassic mass extinction; I/(Ca+Mg)
Corresponding Author:	Tianchen He, Ph.D. University of Leeds Leeds, UNITED KINGDOM
First Author:	Tianchen He, Ph.D.
Order of Authors:	Tianchen He, Ph.D.
	Robert J. Newton
	Paul B. Wignall
	Stephen Reid
	Jacopo Dal Corso
	Satoshi Takahashi
	Hepin Wu
	Simona Todaro
	Pietro Di Stefano
	Vincenzo Randazzo
	Manuel Rigo
	Alexander M. Dunhill
Abstract:	The end-Triassic mass extinction (ETME) was associated with intensified deep-water anoxia in epicontinental seas and mid-depth waters, yet the absolute oxygenation state in the shallow ocean is uncharacterized. Here we report carbonate-associated iodine data from the peritidal Mount Sparagio section (Southern Italy) that documents the ETME (~ 200 Ma) in the western Tethys. We find a sharp drop in carbonate I/(Ca+Mg) ratios across the extinction horizon and persisting into the Early Jurassic. This records local dissolved oxygen and iodate decline in the near-surface ocean of low-latitude Tethys due to the development of depleted oxygen concentrations. Consequently, during the ETME even shallow-water animals, such as the megalodonts seen at Mount Sparagio, were likely the victims of oxygen-poor conditions. The shallow ocean deoxygenation coincides with the synchronous spread of deeper anoxic waters and widespread anoxic deposition on continental shelves and slopes. An upwards expansion of the mid-water oxygen minimum zone in the latest Triassic shoaled the oxycline and triggered a major marine crisis.
Suggested Reviewers:	
Opposed Reviewers:	

Dr Tianchen He
School of Earth and Environment
University of Leeds
Woodhouse Lane
Leeds LS2 9JT
UK
E-mail: T.He@leeds.ac.uk

UNIVERSITY OF LEEDS

FAO: The Editor, *Global and Planetary Change*

Please find accompanying this letter a manuscript entitled '**Shallow ocean oxygen decline during the end-Triassic mass extinction'**, We would like this manuscript to be considered for publication within the '*Paleoenvironmental changes across the Mesozoic–Paleogene hyperthermal events*' Special Issue.

It is suggested that end-Triassic mass extinction (ETME) was closely linked with widespread development of marine anoxia. Yet, the extinction of benthic macrofauna was seen in shallow water locations, where we do not observe any sedimentary or geochemical evidence for anoxic deposition. Hence, it is crucial to track shallow ocean redox state across the ETME, as the shallow ocean ecosystem accounts for the vast majority of aerobic marine organisms and their habitats. Here we present the first iodine concentration profile from the peritidal Mount Sparagio section in Sicily that straddles the mass extinction horizon. Our study is the first measurement of absolute redox state in shallow ocean through the T–J transition using the direct water column redox proxy I/(Ca+Mg).

The key discoveries and outcomes are:

1. We, for the first time, discovered evidence of oxygen decline in the shallowest realms of western Tethys during the ETME.
2. The onset of the shallow ocean deoxygenation event was synchronous with the sudden loss of megalodont bivalves and foraminifer *Triasina hantkeni*, suggesting a cause-and-effect relationship between [O_2] scarcity and ecological stress.
3. We attribute this major redox shift to a combined consequence of local [O_2] decrease and possible upwards expansion of oxygen depletion from mid-depth proximal oxygen minimum zone to the shallow ocean.

The co-authors of this paper acknowledge authorship based on their extensive contribution to this work, and they have approved the final form of this manuscript. No material pertaining to this manuscript is published or under consideration to be published elsewhere.

Many thanks for considering this manuscript for publication in *Global and Planetary Change*.

Yours sincerely,

Tianchen He (corresponding author), on behalf of all co-authors (Robert J. Newton, Paul B. Wignall, Stephen Reid, Jacopo Dal Corso, Satoshi Takahashi, Hepin Wu, Simona Todaro, Pietro Di Stefano, Vincenzo Randazzo, Manuel Rigo & Alexander M. Dunhill

Highlights

- I/(Ca+Mg) profile in a Triassic–Jurassic boundary shallow water carbonate succession of the western Tethys
- Water column hypoxic conditions in the peritidal marine realm during the end-Triassic mass extinction
- Oxygen decline was synchronous with the sudden local loss of benthic macrofauna
- Shallow ocean deoxygenation driven by hyperthermal conditions and upwards expansion of oxygen depletion from mid-depth oxygen minimum zone

Shallow ocean oxygen decline during the end-Triassic mass extinction

Tianchen He[a,*], Robert J. Newton[a], Paul B. Wignall[a], Stephen Reid[a], Jacopo Dal Corso[b], Satoshi Takahashi[c], Hepin Wu[d], Simona Todaro[e], Pietro Di Stefano[e], Vincenzo Randazzo[e], Manuel Rigo[f], Alexander M. Dunhill[a]

[a]*School of Earth and Environment, University of Leeds, Leeds LS2 9JT, UK.*
[b]*State Key Laboratory of Biogeology and Environmental Geology, School of Earth Sciences, China University of Geosciences, Wuhan 430074, China.*
[c]*Department of Earth and Planetary Science, University of Tokyo, Tokyo 113-0033, Japan.*
[d]*State Key Laboratory of Palaeobiology and Stratigraphy & Center for Excellence in Life and Paleoenvironment, Nanjing Institute of Geology and Palaeontology, Chinese Academy of Sciences, Nanjing 210008, China.*
[e]*Department of Earth and Marine Sciences, University of Palermo, Palermo 90123, Italy.*
[f]*Department of Geosciences, University of Padova, Padova 35131, Italy.*

* Corresponding author. *E-mail address:* T.He@leeds.ac.uk (T. He).

ABSTRACT

The end-Triassic mass extinction (ETME) was associated with intensified deep-water anoxia in epicontinental seas and mid-depth waters, yet the absolute oxygenation state in the shallow ocean is uncharacterized. Here we report carbonate-associated iodine data from the peritidal Mount Sparagio section (Southern Italy) that documents the ETME (~ 200 Ma) in the western Tethys. We find a sharp drop in carbonate I/(Ca+Mg) ratios across the extinction horizon and persisting into the Early Jurassic. This records local dissolved oxygen and iodate decline in the near-surface ocean of low-latitude Tethys due to the development of depleted oxygen concentrations. Consequently, during the ETME even shallow-water animals, such as the megalodonts seen at Mount Sparagio, were likely the victims of oxygen-poor conditions. The shallow ocean deoxygenation coincides with the synchronous spread of deeper anoxic waters and widespread anoxic deposition on continental shelves and slopes. An upwards expansion of the mid-water oxygen minimum zone in the latest Triassic shoaled the oxycline and triggered a major marine crisis.

Keywords: Shallow ocean deoxygenation; Western Tethys; End-Triassic mass extinction; I/(Ca+Mg)

1. Introduction

Deoxygenation of the upper ocean is a threat to modern marine ecosystems due to global warming and has been observed as a consequence of past warming events at numerous episodes in Earth history (Jenkyns, 2010; Breitburg et al., 2018; Lu et al., 2018; Oschlies, 2021; Song et al., 2021). The end-Triassic mass extinction (ETME; ~200 Ma) is cotemporaneous with a prominent expansion of marine anoxia that is closely linked to the hothouse climate associated with Central Atlantic Magmatic Province (CAMP) volcanism (Ruhl et al., 2011; He et al., 2020). Existing data demonstrate that strengthened anoxic conditions during the ETME were prevalent across many semi-enclosed basins of Europe (Luo et al., 2018; Beith et al., 2021; Fox et al., 2021) and the mid-depth waters of open ocean (Jost et al., 2017; He et al., 2020), whilst the pelagic deeper ocean remained fully-ventilated (Wignall et al., 2010; Fujisaki et al., 2020). Nevertheless, it is largely unknown with respect to the absolute redox state in the upper water column of shallow marine locations across the Triassic–Jurassic (T–J) transition, as the shallow marine ecosystem accounts for the vast majority of aerobic marine organisms and their habitats. Hence, filling this knowledge gap is crucial for tracking the anoxic/hypoxic-extinction link across the ETME.

Carbonate-associated iodine is widely used as a redox proxy to constrain oxic to hypoxic conditions (dissolved oxygen content [O_2] = ~10 to ~100 μmol/kg) in the upper water column (Lu et al., 2010; Hoogakker et al., 2018; Lu et al., 2018; Pohl et al., 2021). The modern ocean has a relatively uniform concentration of iodine due to its long residence time of ~300 kyr. However, the speciation of iodine in the local water column is dependent upon a redox-sensitive pathway between iodate (IO_3^-) and iodide (I^-) (Luther and Campbell, 1991; Rue et al., 1997). Under low oxygen conditions iodate is reduced to iodide (Luther and Campbell, 1991; Rue et al., 1997), but will immediately convert back to its oxidized form in the presence of abundant dissolved oxygen. Only iodate is readily incorporated into the calcite lattice, substituting for the CO_3^{2-} ion, which allows the concentrations of these structurally substituted iodine to directly reflect water column redox state during the deposition of carbonate (Lu et al., 2010). Thus, the utilization of I/(Ca+Mg) in ancient carbonates affords an opportunity to trace *in situ* [O_2] variations through time in shallow marine environments. Further, carbonate I/(Ca+Mg) can also qualitatively track depth of the oxycline in the water column where the [O_2] decreases more sharply. Carbonate deposited within the shallow ocean realm reflect surface or near-surface seawater dissolved iodate, which is considered as imparted by the expansion or contraction of proximal oxygen minimum zone (OMZ) or the fluctuation of oxycline depth (Zhou et al., 2016; Lu et al., 2018).

Here we present a high-resolution I/(Ca+Mg) record from an upper Rhaetian–lower Hettangian peritidal carbonate succession (Mount Sparagio section, Southern Italy) that was located in the western Tethys (Fig. 1). We show the first evidence of a prominent decline in dissolved oxygen levels in the shallow ocean across the ETME. Low oxygen conditions appear to have persisted into the early Hettangian shallow ocean.

2. Palaeogeography and Stratigraphy

The Mount Sparagio (MS) section from western Sicily (Southern Italy) was located at low-latitude of ~15°N in a shallow carbonate platform of the western Tethys (Fig. 1) (Todaro et al., 2017). The studied succession records upper Rhaetian to lower Hettangian peritidal carbonates (Todaro et al., 2017; He et al., 2020). The subtidal facies of Upper Triassic strata are characterized by the occurrence of megalodontids, calcareous algae and a benthic foraminifera association with *Triasina hantkeni*, *Aulotortus* sp., *Auloconus permodiscoides* indicative of a Rhaetian age (Todaro et al., 2017). The extinction horizon is marked by the last occurrence of megalodontids and the characteristic Rhaetian benthic foraminifer *Triasina hantkeni* and occurs immediately below a thin oolitic limestone that is unique to this level at ~200 m height (Fig. 2). The bloom of the problematic species *Thaumatoporella parvovesiculifera* associated only to rare *Aeolisaccus* sp., at a short distance above this oolitic horizon is a further evidence of the extinction interval, that is followed upward by a slow recovery of the Jurassic benthic community in the earliest Hettangian (Todaro et al., 2018; He et al., 2020).

3. Material and methods

A total of 49 well-preserved micritic limestone samples were measured for carbonate-associated iodine concentration. Bulk carbonate rocks were cut into small rock cubes to trim the weathered crust. This was followed by grinding to a fine powder using a TEMA laboratory agate disc mill. Around 20 mg of sample powder was first rinsed by ultrapure water three times and dried. For each sample approximately 5 mg of cleaned dry powder was then weighed and treated with 3 % (v/v) nitric acid using an ultrasonic bath at room temperature. This carbonate leaching step was completed within 15 minutes to minimize the potential for iodine escape at low pH conditions. The samples were centrifuged and the supernatant containing the leachate was mixed with a 0.5 % (v/v) HNO_3, 0.5 % (v/v) ammonium hydroxide, 3 % (v/v) methanol solution. The ammonium hydroxide is required to stabilize the iodine in solution and minimize sample washout times during inductively coupled plasma mass spectrometer (ICP-MS) analysis. The methanol promotes a signal enhancement for iodine measurements using ICP-MS (Ariga et al., 2019). Analysis of these solutions must be complete within 24 hours of dissolution. An aliquot was measured for concentrations of Ca and Mg using a ThermoFisher iCAP 7400 radial inductively coupled plasma optical emission spectrometer (ICP-OES). Samples and calibration standards were internally standardized using 1 mg L^{-1} Y and Lu. A further aliquot was analysed for iodine using a ThermoFisher iCAP Qc ICP-MS in the Aqueous Analytical Facility, University of Leeds. Samples and calibration standards were internally standardized using 5 mg L^{-1} Te and the standards matrixed matched to the samples by addition of 50 mg L^{-1} Ca. The instrumental precisions for Ca, Mg and I are better than 1 %. The ICP-MS was tuned for highest sensitivity to iodine. Repeated measurements of the reference material JCp-1 (coral, *Porites* sp.) yielded a carbonate-associated iodine concentration of 5.48 ± 0.17 µg/g, n=14 (see Table S1 for JCp-1 measurement data), comparable to the published acid-leachable iodine concentration of 5.43 ± 0.07 µg/g, n=8 (Lu et al., 2010) and the certified total measure of iodine concentration of 5.5 ± 0.2 µg/g, n=5 (Chai and Muramatsu, 2007).

4. Results and discussions

We first rule out potential lithological and diagenetic controls on the I/(Ca+Mg) dataset. Samples are dominantly micritic limestone with uniform $CaCO_3$ contents mostly above 90% and lean in organic matter (He et al., 2020), suggesting minimal contamination by non-carbonate phase and organics-bounded iodine (Glock et al., 2019). No correlation is observed with the Mg/Ca or Mn/Sr (Fig. 3), which indicates a minor influence of dolomitization or diagenetic imprint on the structurally incorporated iodine. Hence, the carbonate I/(Ca+Mg) changes at the MS section likely indicate primary signals of water column redox conditions (Lu et al., 2010).

Our I/(Ca+Mg) profile from MS section documents higher baseline values with an average of 3.5 µmol/mol throughout the pre-extinction period in the late Rhaetian (Fig. 2a). These new I/(Ca+Mg) data add to the existing low-resolution global data compilation for the T–J transition (~200 Ma) (Lu et al., 2018) when seawater iodine concentration depicts a substantial rise from the low plateau phase (~1 µmol/mol) in the Permian–Triassic to high levels (~3 µmol/mol) in the Early Jurassic. Hence, our I/(Ca+Mg) data from MS section validate the previous finding of a long-term increase of oceanic I/Ca ratios from the Triassic to the Jurassic. This change was attributed to a net reduction of oxygen consumption in the upper ocean due to post-ETME radiation of modern-type eukaryotic phytoplankton (Lu et al., 2018).

Nevertheless, the absolute I/(Ca+Mg) values at MS section fluctuate between 2 µmol/mol and 6 µmol/mol throughout the pre-ETME late Rhaetian (Fig. 2a). This fluctuating I/(Ca+Mg) record may have resulted from a periodic shallowing of the depositional site (Fig. 2a), which is consistent with facies stacking evidence of shallowing-upward cycles (subtidal-intertidal-supratidal) in these peritidal sediments (Todaro et al., 2017). Alternatively, fluctuation in seawater iodine abundance may have been driven by frequent shallowing of water column oxycline that overlies a proximal OMZ, where dissolved iodate were completely reduced to iodide (Zhou et al., 2016; Lu et al., 2018).

In stark contrast to the pre-extinction interval, I/(Ca+Mg) data record a sharp decline from ~5 μmol/mol to below 1 μmol/mol in the latest Rhaetian (Fig. 2a), which coincides precisely with the mass extinction horizon. The extinction is also characterized by the sudden disappearance of megalodont bivalves and the foraminifer *Triasina hantkeni*, and a synchronous positive S-isotope excursion in carbonate-associated sulfate ($\delta^{34}S_{CAS}$; Fig. 2b). Hyperthermal conditions around the T–J transition are thought to have initiated the spread of marine anoxia via increased eutrophication, oxygen consumption and reduction in oxygen solubility in warmer surface waters (He et al., 2020). The large decrease in carbonate I/(Ca+Mg) ratios across the ETME (MS) indicates a depletion of the dissolved iodate pool due to decreased [O_2]. The concurrent positive $\delta^{34}S_{CAS}$ shift suggests extensive anoxia and burial of pyrite on continental shelves and slopes at this time (He et al., 2020). The spread of anoxic waters would have been enhanced by oceanic sulfate paucity, which would have suppressed the anaerobic oxidation of methane in the sediments, leading to increased benthic methane flux and net oxygen consumption on the seafloor (He et al., 2020). Anoxic conditions likely expanded from the mid-depth OMZ into shallower waters (Fig. 4b), causing hypoxia and iodate depletion in the surface waters. Thus, the shallowing of the oxycline and upwards invasion of anoxic waters across the ETME is likely to explain the sharp decline in carbonate I/(Ca+Mg) ratios. Indeed, uranium isotope evidence for contemporary deeper water anoxia was found in the adjacent Lombardy Basin (Jost et al., 2017), which likely suggests an upwards expansion of OMZ across the ETME in the area.

The I/(Ca+Mg) record stays at low level (1.6 μmol/mol on average) across the T–J boundary and into the earliest Hettangian (Fig. 2a), indicating continued iodate depletion due to hypoxic conditions in the shallow ocean. However, these post-ETME carbonates exhibit slightly higher iodine concentration compared to those at the major phase of ETME, which may indicate a lesser degree or persistency of hypoxia. Further, the uppermost Rhaetian–lower Hettangian sedimentology of the MS section records a minor facies transition to relatively deeper peritidal setting, evident by the thin oolitic limestone bed at a flooding surface immediately above the extinction horizon and higher occurrence of marly limestone in the lower Hettangian (Fig. 2). Hence, it is possible that MS section saw a transition to slight deeper facies preceding the ETME, so better connection to the open ocean. Thus, the shallow ocean hypoxic condition revealed from the post-extinction MS section likely indicates an open marine signal of dysoxia. These commonly hypoxic conditions likely prevailed in the wider shallow ocean in the post-extinction early Hettangian, possibly with an oscillating redox state as seen in the European epicontinental sea (Beith et al., 2021; Fox et al., 2021). The shallow ocean hypoxia during the T–J transition may have also varied spatially although uranium isotope evidence suggests deeper water column anoxia was widespread until the middle Hettangian Stage (Jost et al., 2017). Despite persistent low oxygen levels in the post-ETME shallow ocean, it did not prolong the extinction or inhibit the local recovery of marine communities (Fig. 2). Some other environmental stressors for ETME, such as ocean acidification (Fox et al., 2020, 2021), may have receded immediately after the extinction, allowing the shallow ocean ecosystem to recover in the early Hettangian.

In summary, our new I/(Ca+Mg) record from the MS section in Southern Italy, combined with published $\delta^{34}S_{CAS}$ data indicate evidence of oxygen decline in the shallowest realms of western Tethys during the ETME. We attribute this major redox shift to a combined consequence of local [O_2] decrease and possible upwards expansion of oxygen depletion from mid-depth OMZ to the shallow ocean. The onset of the shallow ocean deoxygenation event was clearly synchronous with the loss of megalodont bivalves and foraminifer *Triasina hantkeni* (Fig. 2), suggesting a cause-and-effect relationship between [O_2] scarcity and ecological stress even in exceptionally shallow-water Tethyan areas. This adds to the growing evidence that indicates a global anoxia/hypoxia-extinction link in a variety of marine settings during the ETME (Jaraula et al., 2013; Jost et al., 2017; Luo et al., 2018; He et al., 2020; Beith et al., 2021; Fox et al., 2021; Kipp and Tissot, 2022). Many similar events through the Mesozoic and Paleogene (e.g., Toarcian oceanic anoxic event, Paleocene-Eocene Thermal Maximum) were accompanied by hyperthermal events and upper ocean hypoxia (Jenkyns, 2010; Lu et al., 2010; Zhou et al., 2014, 2016; Song et al., 2021), which together serve as potential analogues to inform possible outcomes of ongoing anthropogenic warming.

Declaration of competing interest

The authors declare that they have no known competing financial interests or personal relationships that could have appeared to influence the work reported in this paper.

Acknowledgements

This work was supported by the Natural Environment Research Council (grant NE/N018559/1) to RJN, the National Natural Science Foundation of China (41888101, 41902026) to TH and HW, and a Leverhulme Early Career Fellowship (ECF-2015-044) to AMD. We also acknowledge funding from the International Continental Scientific Drilling Program. This manuscript is a contribution to the Integrated Understanding of the Early Jurassic Earth System and Timescale (JET) project and the UNESCO IGCP 739. E.C. Turner is acknowledged for assistance in the field work. We thank F. Bowyer, S. W. Poulton and Y. Xiong for valuable discussions during method development.

Appendix A. Supplementary data

Supplementary data to this article can be found at Supplementary Data 1.

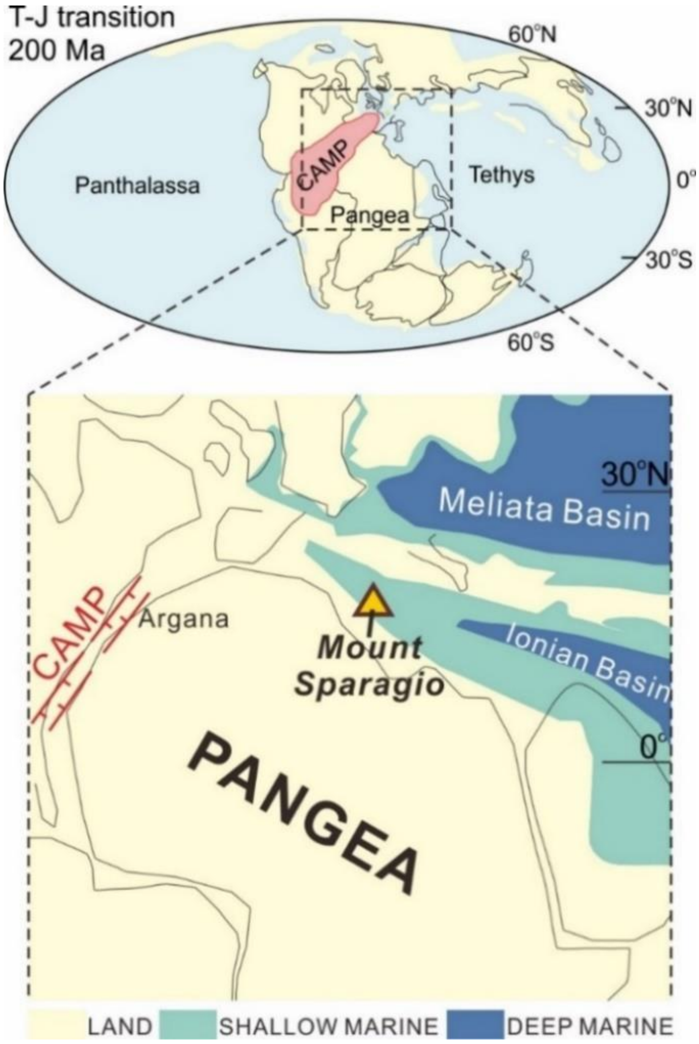

Fig. 1. Paleogeographic map for the shallow marine Mount Sparagio section of western Tethys during the Triassic–Jurassic (T–J) transition. This map is based on Todaro *et al.* (2018). Yellow triangle indicates the location of the studied Mount Sparagio section. CAMP: Central Atlantic Magmatic Province.

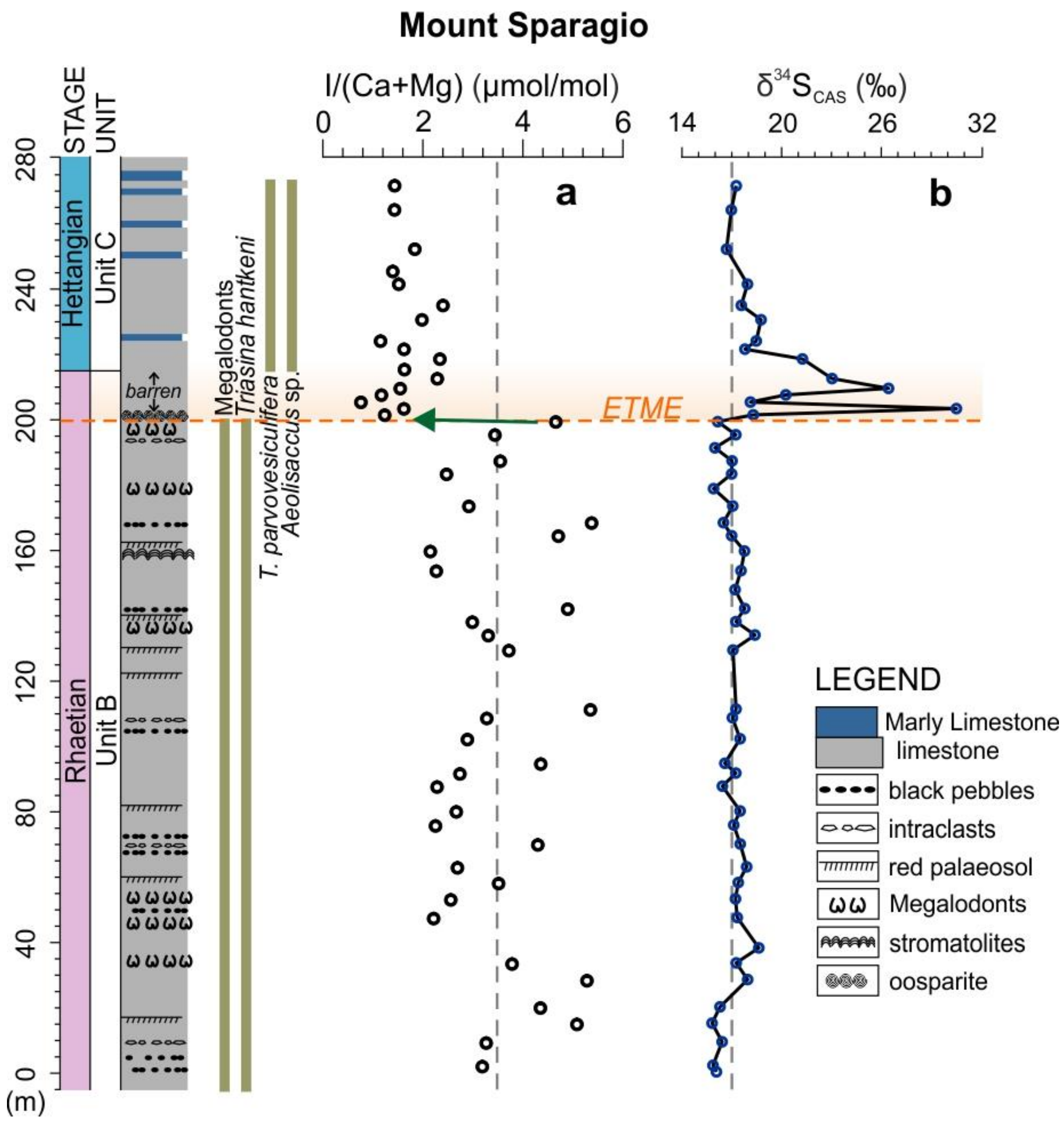

Fig. 2. I/(Ca+Mg) and $\delta^{34}S_{CAS}$ profiles of Mount Sparagio section from Latest Triassic to Early Jurassic. Stratigraphic depth (m) and the lithological log are presented alongside the stages, with stratigraphic units of Todaro *et al.* (2018). Carbonate-associated sulfate $\delta^{34}S_{CAS}$ data are from He *et al.* (2020). The orange horizontal dash line and shadowed field indicate the end-Triassic mass extinction (ETME) at this location. The green arrow indicates the sharp drop in I/(Ca+Mg) across the ETME. Vertical dash lines indicate pre-extinction average values of I/(Ca+Mg) and $\delta^{34}S_{CAS}$.

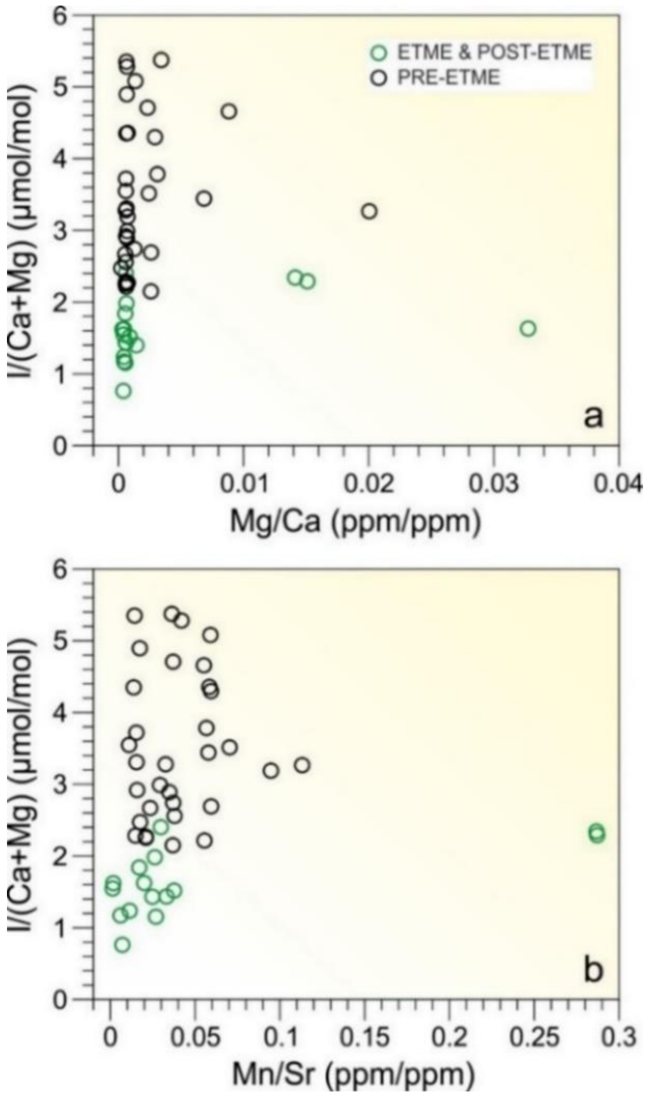

Fig. 3. Correlation between I/(Ca+Mg) molar ratios and elemental mass ratios of carbonates from Mount Sparagio section. a Cross-plot of I/[Ca+Mg] and Mg/Ca shows no correlation ($R^2 < 0.001$), suggesting no alteration of redox-proxy values from minor dolomitization (Mg/Ca < 0.04). **b** Cross-plot of I/[Ca+Mg] and Mn/Sr displays no correlation ($R^2 = 0.002$), suggesting minimal diagenetic imprint. Mn and Sr data are from He *et al.* (2020). ETME: end-Triassic mass extinction.

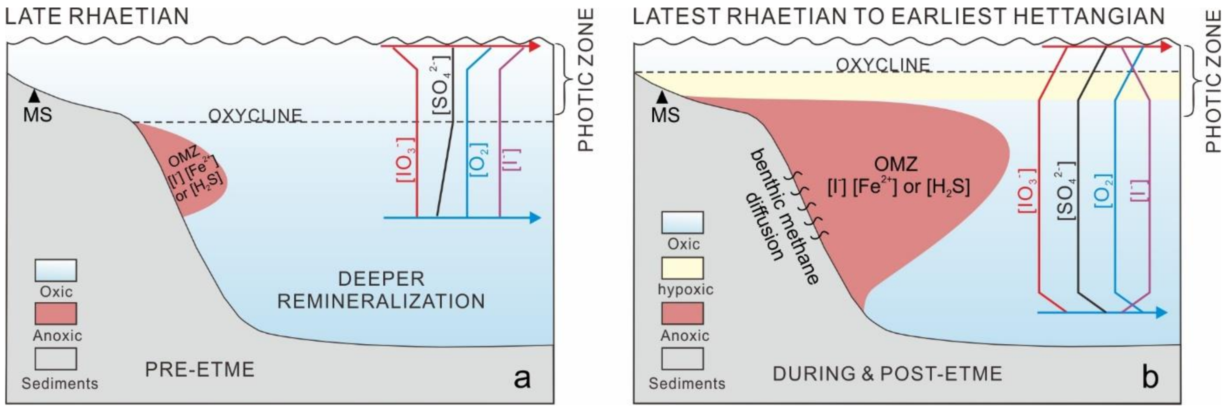

Fig. 4. Schematic diagram of global oceanic redox change through the Triassic–Jurassic transition. Iodine speciation systematics is adapted from Lu *et al.* (2018). Relative concentrations of redox-sensitive elements: iodate (IO_3^-), iodide (I^-) and sulfate (SO_4^{2-}) are indicated. OMZ: Oxygen Minimum Zone. Anoxic-ferruginous and euxinic water column conditions are demarcated with [Fe^{2+}] and [H_2S] respectively. ETME: end-Triassic mass extinction. **a** Pre-ETME 'Mesozoic-type' water column redox state with well-oxygenated upper ocean and restricted OMZ in mid-depth waters. **b** Redox state during and post-ETME showing an expanded OMZ and shallowing of the oxycline, leading to hypoxic conditions and iodate depletion in the shallow ocean. Low sulfate concentration in the ocean likely promoted increased benthic methane flux to the bottom-water and oxygen demand in OMZ (He et al., 2020).

References

Ariga, T., Zhu, Y., Inagaki, K., 2019. Study on carbon-induced signal enhancement in inductively coupled plasma mass spectrometry: an approach from the spatial distribution of analyte signal intensities. J. Anal. At. Spectrom. 34, 1865–1874. https://doi.org/10.1039/C9JA00152B

Beith, S.J., Fox, C.P., Marshall, J.E.A., Whiteside, J.H., 2021. Recurring photic zone euxinia in the northwest Tethys impinged end-Triassic extinction recovery. Palaeogeogr. Palaeoclimatol. Palaeoecol. 584, 110680. https://doi.org/10.1016/j.palaeo.2021.110680

Breitburg, D., Levin, L.A., Oschlies, A., Grégoire, M., Chavez, F.P., Conley, D.J., Garçon, V., Gilbert, D., Gutiérrez, D., Isensee, K., Jacinto, G.S., Limburg, K.E., Montes, I., Naqvi, S.W.A., Pitcher, G.C., Rabalais, N.N., Roman, M.R., Rose, K.A., Seibel, B.A., Telszewski, M., Yasuhara, M., Zhang, J., 2018. Declining oxygen in the global ocean and coastal waters. Science . 359. https://doi.org/10.1126/science.aam7240

Chai, J.Y., Muramatsu, Y., 2007. Determination of Bromine and Iodine in Twenty-three Geochemical Reference Materials by ICP-MS. Geostand. Geoanalytical Res. 31, 143–150. https://doi.org/10.1111/j.1751-908X.2007.00856.x

Fox, C.P., Cui, X., Whiteside, J.H., Olsen, P.E., Summons, R.E., Grice, K., 2020. Molecular and isotopic evidence reveals the end-Triassic carbon isotope excursion is not from massive exogenous light carbon. Proc. Natl. Acad. Sci. U. S. A. 117, 30171–30178. https://doi.org/10.1073/pnas.1917661117

Fox, C.P., Whiteside, J., Olsen, P.E., Cui, X., Summons, R.E., Idiz, E., Grice, K., 2021. Two-pronged kill mechanism at the end-Triassic mass extinction. Geology in press.

Fujisaki, W., Fukami, Y., Matsui, Y., Sato, T., Sawaki, Y., Suzuki, K., 2020. Redox conditions and nitrogen cycling during the Triassic-Jurassic transition: A new perspective from the mid-Panthalassa. Earth-Science Rev. 204, 103173. https://doi.org/10.1016/j.earscirev.2020.103173

Glock, N., Liebetrau, V., Vogts, A., Eisenhauer, A., 2019. Organic heterogeneities in foraminiferal calcite traced through the distribution of N, S, and I measured with nanosims: A new challenge for element-ratio-based paleoproxies? Front. Earth Sci. 7, 1–14. https://doi.org/10.3389/feart.2019.00175

He, T., Dal Corso, J., Newton, R.J., Wignall, P.B., Mills, B.J.W., Todaro, S., Di Stefano, P., Turner, E.C., Jamieson, R.A., Randazzo, V., Rigo, M., Jones, R.E., Dunhill, A.M., 2020. An enormous sulfur isotope excursion indicates marine anoxia during the end-Triassic mass extinction. Sci. Adv. 6, eabb6704. https://doi.org/10.1126/sciadv.abb6704

Hoogakker, B.A.A., Lu, Z., Umling, N., Jones, L., Zhou, X., Rickaby, R.E.M., Thunell, R., Cartapanis, O., Galbraith, E., 2018. Glacial expansion of oxygen-depleted seawater in the eastern tropical Pacific. Nature 562, 410–413. https://doi.org/10.1038/s41586-018-0589-x

Jaraula, C.M.B., Grice, K., Twitchett, R.J., Böttcher, M.E., LeMetayer, P., Dastidar, A.G., Opazo, L.F., 2013. Elevated pCO2 leading to Late Triassic extinction, persistent photic zone euxinia, and rising sea levels. Geology 41, 955–958. https://doi.org/10.1130/G34183.1

Jenkyns, H.C., 2010. Geochemistry of oceanic anoxic events. Geochemistry, Geophys. Geosystems 11, 1–30. https://doi.org/10.1029/2009GC002788

Jost, A.B., Bachan, A., van de Schootbrugge, B., Lau, K. V., Weaver, K.L., Maher, K., Payne, J.L., 2017. Uranium isotope evidence for an expansion of marine anoxia during the end-Triassic extinction. Geochemistry, Geophys. Geosystems 18, 3093–3108. https://doi.org/10.1002/2017GC006941

Kipp, M.A., Tissot, F.L.H., 2022. Inverse methods for consistent quantification of seafloor anoxia using uranium isotope data from marine sediments. Earth Planet. Sci. Lett. 577, 117240. https://doi.org/10.1016/j.epsl.2021.117240

Lu, W., Ridgwell, A., Thomas, E., Hardisty, D.S., Luo, G., Algeo, T.J., Saltzman, M.R., Gill, B.C., Shen, Y., Ling, H., Edwards, C.T., Whalen, M.T., Zhou, X., Gutchess, K.M., Jin, L., Rickaby, R.E.M., Jenkyns, H.C., Lyons, T.W., Lenton, T.M., Kump, L.R., Lu, Z., 2018. Late inception of a resiliently oxygenated upper ocean. Science. 5372, eaar5372. https://doi.org/10.1126/science.aar5372

Lu, Z., Jenkyns, H.C., Rickaby, R.E.M., 2010. Iodine to calcium ratios in marine carbonate as a paleo-redox proxy during oceanic anoxic events. Geology 38, 1107–1110. https://doi.org/10.1130/G31145.1

Luo, G., Richoz, S., van de Schootbrugge, B., Algeo, T.J., Xie, S., Ono, S., Summons, R.E., 2018. Multiple sulfur-isotopic evidence for a shallowly stratified ocean following the Triassic-Jurassic boundary mass extinction. Geochim. Cosmochim. Acta 231, 73–87. https://doi.org/10.1016/j.gca.2018.04.015

Luther, G.W., Campbell, T., 1991. Iodine speciation in the water column of the Black Sea. Deep Sea Res. Part A. Oceanogr. Res. Pap. 38, S875–S882. https://doi.org/10.1016/S0198-0149(10)80014-7

Oschlies, A., 2021. A committed fourfold increase in ocean oxygen loss. Nat. Commun. 12, 2307. https://doi.org/10.1038/s41467-021-22584-4

Pohl, A., Lu, Z., Lu, W., Stockey, R.G., Elrick, M., Li, M., Desrochers, A., Shen, Y., He, R., Finnegan, S., Ridgwell, A., 2021. Vertical decoupling in Late Ordovician anoxia due to reorganization of ocean circulation. Nat. Geosci. 14, 868–873. https://doi.org/10.1038/s41561-021-00843-9

Rue, E.L., Smith, G.J., Cutter, G.A., Bruland, K.W., 1997. The response of trace element redox couples to suboxic conditions in the water column. Deep Sea Res. Part I Oceanogr. Res. Pap. 44, 113–134. https://doi.org/10.1016/S0967-0637(96)00088-X

Ruhl, M., Bonis, N.R., Reichart, G.-J., Damsté, J.S.S., Kürschner, W.M., 2011. Atmospheric Carbon Injection Linked to End-Triassic Mass Extinction. Science. 333, 430–434. https://doi.org/10.1126/science.1204255

Song, Haijun, Kemp, D.B., Tian, L., Chu, D., Song, Huyue, Dai, X., 2021. Thresholds of temperature change for mass extinctions. Nat. Commun. 12, 4694. https://doi.org/10.1038/s41467-021-25019-2

Todaro, S., Di Stefano, P., Zarcone, G., Randazzo, V., 2017. Facies stacking and extinctions across the Triassic–Jurassic boundary in a peritidal succession from western Sicily. Facies 63, 20. https://doi.org/10.1007/s10347-017-0500-5

Todaro, S., Rigo, M., Randazzo, V., Di Stefano, P., 2018. The end-Triassic mass extinction: A new correlation between extinction events and $\delta^{13}C$ fluctuations from a Triassic-Jurassic peritidal succession in western Sicily. Sediment. Geol. 368, 105–113. https://doi.org/10.1016/j.sedgeo.2018.03.008

Wignall, P.B., Bond, D.P.G., Kuwahara, K., Kakuwa, Y., Newton, R.J., Poulton, S.W., 2010. An 80 million year oceanic redox history from Permian to Jurassic pelagic sediments of the Mino-Tamba terrane, SW Japan, and the origin of four mass extinctions. Glob. Planet. Change 71, 109–123. https://doi.org/10.1016/j.gloplacha.2010.01.022

Zhou, X., Thomas, E., Rickaby, R.E.M., Winguth, A.M.E., Lu, Z., 2014. I/Ca evidence for upper ocean deoxygenation during the PETM. Paleoceanography 29, 964–975. https://doi.org/10.1002/2014PA002702

Zhou, X., Thomas, E., Winguth, A.M.E., Ridgwell, A., Scher, H., Hoogakker, B.A.A., Rickaby, R.E.M., Lu, Z., 2016. Expanded oxygen minimum zones during the late Paleocene-early Eocene: Hints from multiproxy comparison and ocean modeling. Paleoceanography 31, 1532–1546. https://doi.org/10.1002/2016PA003020

Sample name	Depth m	I/(Ca+Mg) µmol/mol	Mg/Ca w/w	Mn/Sr w/w
SP2	2.0	3.2	0.0007	0.095
SP4	9.2	3.3	0.0200	0.113
SP8	14.9	5.1	0.0014	0.059
SP12	19.9	4.3	0.0006	0.014
SP17	28.3	5.3	0.0007	0.042
SP19	33.4	3.8	0.0031	0.057
SP26	47.3	2.2	0.0006	0.056
SP29	53.0	2.6	0.0006	0.038
SP32	58.0	3.5	0.0024	0.070
SP36	62.8	2.7	0.0026	0.059
SP38	69.8	4.3	0.0029	0.059
SP41	75.6	2.3	0.0006	0.021
SP43	79.9	2.7	0.0005	0.023
SP46.5	87.5	2.3	0.0006	0.015
SP48	91.5	2.7	0.0013	0.037
SP49.5	94.5	4.4	0.0007	0.058
SP51	102.0	2.9	0.0007	0.035
SP53.5	108.4	3.3	0.0006	0.033
SP55	111.0	5.3	0.0006	0.014
SP60	129.1	3.7	0.0006	0.015
SP63	133.7	3.3	0.0007	0.015
SP65	137.8	3.0	0.0007	0.029
SP67	141.8	4.9	0.0007	0.017
SP73	153.4	2.3	0.0008	0.021
SP76	159.4	2.1	0.0026	0.037
SP78	164.1	4.7	0.0023	0.037
SP80	168.1	5.4	0.0034	0.036
SP82	173.2	2.9	0.0006	0.016
SP86	183.0	2.5	0.0002	0.018
SP88	187.0	3.5	0.0006	0.011
SP92	195.0	3.4	0.0068	0.058
SP94	199.0	4.7	0.0088	0.055
SP95	201.1	1.2	0.0004	0.011
SP96	203.0	1.6	0.0003	0.002
SP97	205.0	0.8	0.0004	0.007
SP98	207.2	1.2	0.0005	0.006
SP99	209.2	1.5	0.0004	0.001
SP100	212.2	2.3	0.0151	0.287
SP102	215.0	1.6	0.0327	
SP103	218.2	2.3	0.0141	0.287
SP104	221.2	1.6	0.0005	0.020
SP105	223.7	1.2	0.0006	0.027
SP108	230.2	2.0	0.0006	0.026
SP110	234.6	2.4	0.0006	0.030
SP113	241.1	1.5	0.0009	0.038
SP115	245.0	1.4	0.0014	
SP118	251.8	1.8	0.0005	0.017
SP123	263.8	1.4	0.0006	0.025
SP126	271.2	1.4	0.0006	0.033

Measurements	Iodine µg/g
1	5.22
2	5.44
3	5.33
4	5.38
5	5.59
6	5.67
7	5.47
8	5.70
9	5.47
10	5.72
11	5.37
12	5.64
13	5.59
14	5.19
average	5.48
std	0.17

Figure 1

Click here to access/download;Figure;Figure 1.jpg

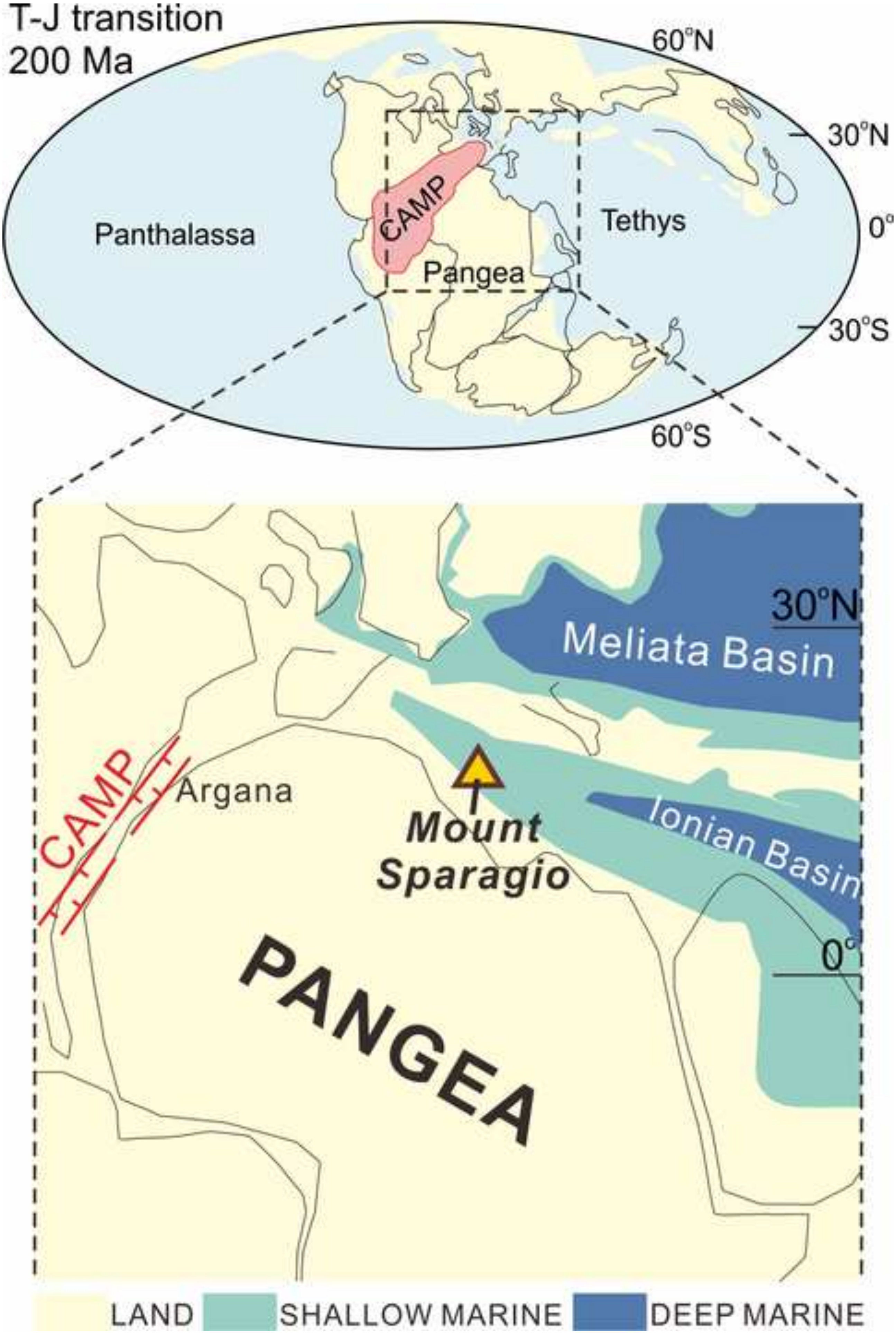

Figure 2

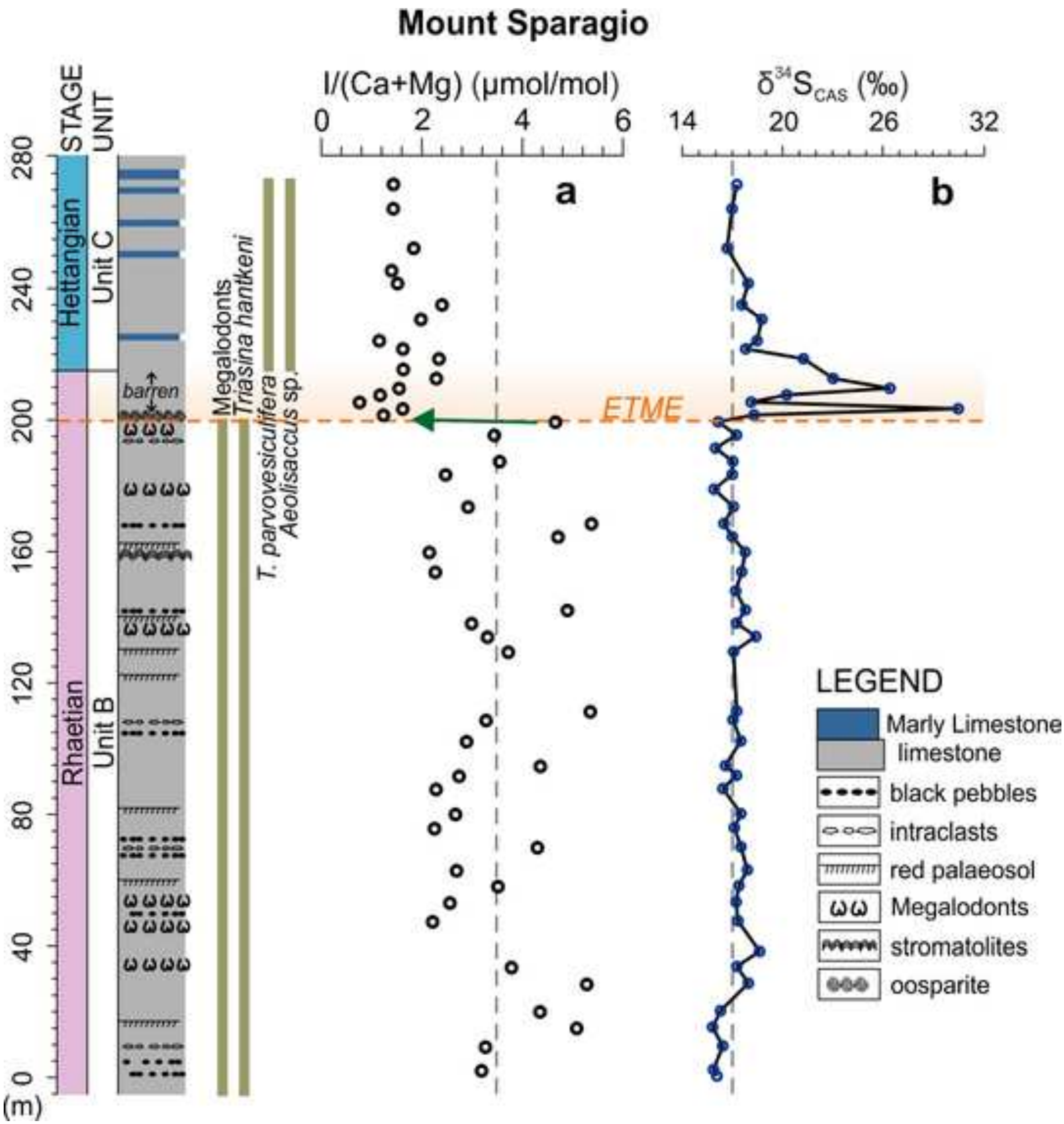

Mount Sparagio
STAGE
UNIT
I/(Ca+Mg) (μmol/mol)
0
2
4
6
δ34SCAS (‰)
14
20
26
32
a
b
280
240
200
160
120
80
40
0
(m)
Hettangian
Unit C
Rhaetian
Unit B
barren
Megalodonts
Triasina hantkeni
T. parvovesiculifera
Aeolisaccus sp.
ETME
LEGEND
Marly Limestone
limestone
black pebbles
intraclasts
red palaeosol
Megalodonts
stromatolites
oosparite

Figure 3

Click here to access/download;Figure;Figure 3.jpg

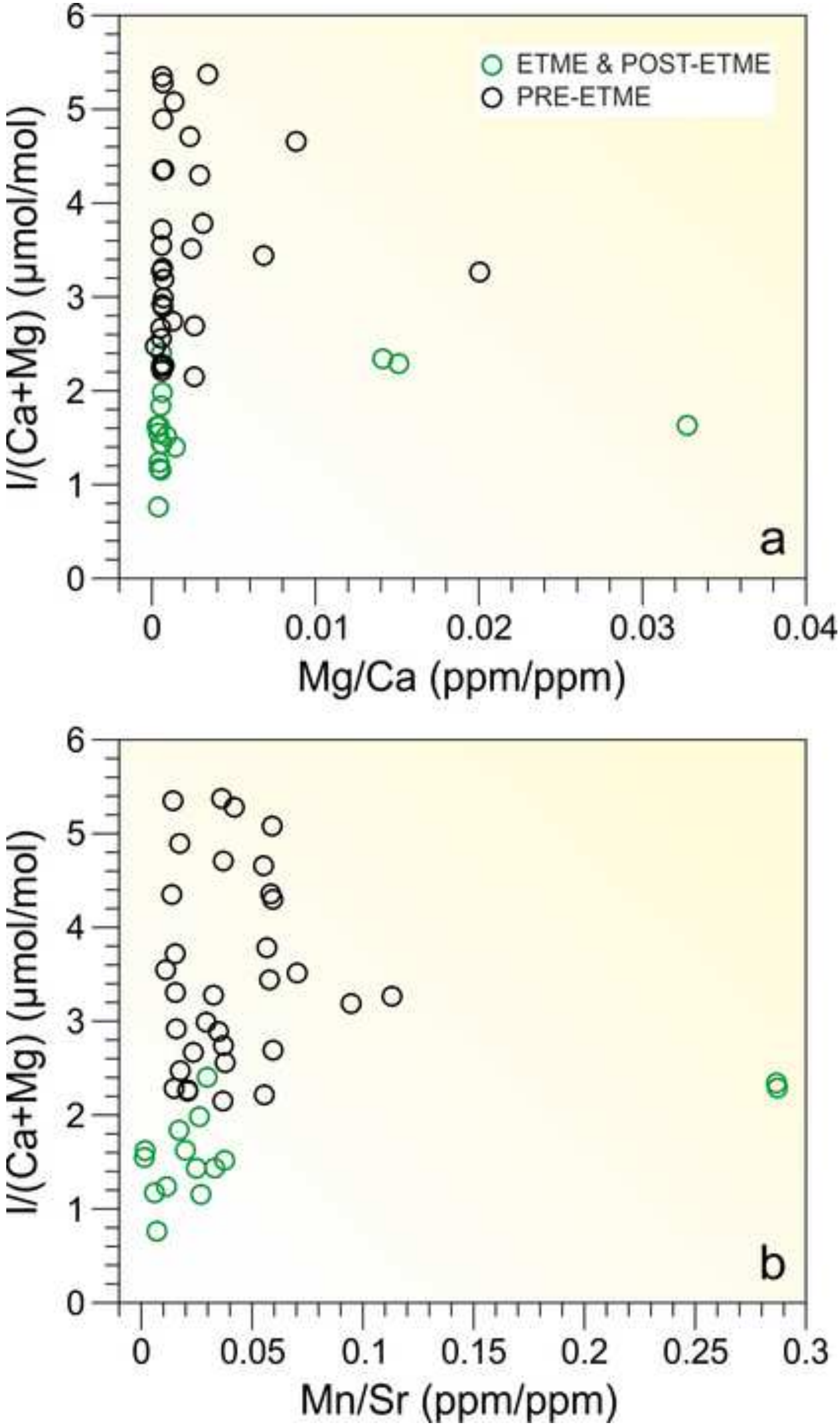

Figure 4

Click here to access/download;Figure;Figure 4.jpg